19

Thermodynamics of ABO_3-Type Perovskite Surfaces

Eugene Heifets[1], Eugene A. Kotomin[1,2], Yuri A. Mastrikov[2], Sergej Piskunov[3] and Joachim Maier[1]

[1]*Max Planck Institute for Solid State Research, Stuttgart,*
[2]*Institute of Solid State Physics, University of Latvia, Riga,*
[3]*Department of Computer Science, University of Latvia, Riga,*
[1]*Germany*
[2,3]*Latvia*

1. Introduction

The ABO_3-type perovskite manganites, cobaltates, and ferrates (A= La, Sr, Ca; B=Mn, Co, Fe) are important functional materials which have numerous high-tech applications due to their outstanding magnetic and electrical properties, such as colossal magnetoresistance, half-metallic behavior, and composition-dependent metal-insulator transition (Coey et al., 1999; Haghiri-Gosnet & Renard, 2003). Owing to high electronic and ionic conductivities. these materials show also excellent electrochemical performance, thermal and chemical stability, as well as compatibility with widely used electrolyte based on yttrium-stabilized zirconia (YSZ). Therefore they are among the most promising materials as cathodes in solid oxide fuel Cells (SOFCs) (Fleig et al., 2003) and gas-permeation membranes (Zhou, 2009). Many of the above-mentioned applications require understanding and control of surface properties. An important example is $LaMnO_3$ (LMO). Pure LMO has a cubic structure above 750 K, whereas below this temperature the crystalline structure is orthorhombic, with four formula units in a primitive cell. Doping of LMO with Sr allows one to increase both the ionic and electronic conductivity as well as to stabilize the cubic structure down to room temperatures - necessary conditions for improving catalytic performance of LMO in electrochemical devices, e.g. cathodes for SOFCs. In optimal compositions of $La_{1-x_b}Sr_{x_b}MnO_3$ (LSM) solid solution the bulk concentration of Sr reaches $x_b \approx 0.2$.

Understanding of LMO and LSM basic properties (first of all, energetic stability and reactivity) for pure and adsorbate-covered surfaces is important for both the low-temperature applications (e.g., spintronics) and for high-temperature electrochemical processes where understanding the mechanism of oxygen reduction on the surfaces is a key issue in improving the performance of SOFC cathodes and gas-permeation membranes at relatively high (~800 C) temperatures. First of all, it is necessary to determine which LMO/LSM surfaces are the most stable under operational conditions and which terminations are the energetically preferential? For example, the results of our simulations described below show that the [001] surfaces are the most stable ones in the case of LMO (as

compared to [011] and others). However, the [001] surfaces have, in turn, two different terminations: LaO or MnO_2. We will compare stabilities of these terminations under different environmental conditions (temperature and partial pressure of oxygen gas). Another important question to be addressed is, how Sr doping affects relative stabilities of the LMO surfaces? These issues directly influence the SOFC cathode performance. Answering these questions requires a thermodynamic analysis of surfaces under realistic SOFC operational conditions which is in the main focus of this Chapter. Such a thermodynamic analysis is becoming quite common in investigating structure and stability of various crystal surfaces (Examples of thermodynamic analyses of binary and ternary compounds can be found in Reuter & Scheffler, 2001a, 2001b; Bottin et al., 2003; Heifets et al., 2007a, 2007b, Johnson et al., 2004).

The thermodynamic analysis requires careful calculations of energies for two-dimensional slabs terminated by surfaces with various orientations and terminations. The required energies could be calculated using *ab initio* methods of the atomic and electronic structure based on density functional theory (DFT). In this Chapter, we present the results obtained using two complementary *ab initio* DFT approaches employing two different types of basis sets (BS) representing the electronic density distribution: plane waves (PW) and linear combination of atomic orbitals (LCAO). Both techniques were used to calculate the atomic and electronic structures of a pure LMO whereas investigation of the Sr influence on the stability of different (001) surfaces was performed within LCAO approach.

After studying the stabilities of various surfaces, the next step is investigating the relevant electrochemical processes on the most stable surfaces. For this purpose, we have to evaluate the adsorption energies for O_2 molecules, O atoms, the formation energies of O vacancies in the bulk and at the stable perovskite surfaces. These energies, together with calculated diffusion barriers of these species and reactions between them, allow us to determine the mechanism of incorporation of O atoms into the cathode materials. However, such mechanistic and kinetic analyses lie beyond the scope of this Chapter (for more details see e.g. Mastrikov et al., 2010). Therefore, we limit ourselves here only to the thermodynamic characterization of the initial stages of the oxygen incorporation reaction, which include formation of stable adsorbed species (adsorbed O atoms, O_2 molecules) and formation of oxygen vacancies. The data for formation of both oxygen vacancies and adsorbed oxygen atoms and molecules have been collected using plane wave based DFT.

2. Computational details

The employed thermodynamic analysis relies on the energies obtained by DFT computations of the electronic structure of slabs terminated by given surfaces using the above-mentioned two types of basis sets. All calculations are performed with spin-polarized electronic densities, complete neglect of spin polarization results in considerable errors in material properties (Kotomin et al, 2008)).

The plane wave calculations were performed with VASP 4.6.19 code (Kresse & Hafner, 1993; Kresse & Furthmüller, 1996; Kresse et al., 2011), which implements projector augmented wave (PAW) technique (Bloechl, 1994; Kresse & Joubert, 1999), and generalized gradient approximation (GGA) exchange-correlation functional proposed by Perdew and Wang (PW91) (Perdew et al., 1992) . Calculations were done with the cut-off energy of 400 eV. The core orbitals on all atoms were described by PAW pseudopotentials, while electronic

wavefunctions of valence electrons on O atoms and valence and core-valence electrons on metal atoms were explicitly evaluated in our calculations.

We found that seven- and eight-plane *slabs* infinite in two (x-y) directions are thick enough to show convergence of the main properties. The periodically repeated slabs were separated along the z-axis by a large vacuum gap of 15.8 Å. All atomic coordinates in slabs were allowed to relax. To avoid problems with a slab dipole moment and to ensure having identical surfaces on both sides of slabs, we employed the symmetrical seven-layer slab $MnO_2(LaO\text{-}MnO_2)_3$ in our plane-wave simulations, even though it has a Mn excess relative to La and a higher oxygen content. Such a choice of the slab structure however only slightly changes the calculated energies. For example, the energy for dissociative oxygen adsorption on the [001] MnO_2-terminated surface

$$O_2 + 2Mn_{Mn}^{x} \rightleftharpoons 2O_{ad}^{-} + 2Mn_{Mn}^{\bullet} \tag{1}$$

is -2.7 eV for eight-layers $(LaO\text{-}MnO_2)_4$ slab and -2.2 eV for the symmetrical seven-layer $MnO_2\text{-}(LaO\text{-}MnO_2)_3$ slab. The use of symmetrical slabs also allows decoupling the effects of different surface terminations and saving computational time due to the possibility to exploit higher symmetry of the slabs. The simulations were done using an extended $2\sqrt{2} \times 2\sqrt{2}$ surface unit cell and a 2 × 2 Monkhorst-Pack k-point mesh in the Brillouin zone (Monkhorst & Pack, 1976). Such a unit cell corresponds to 12.5% concentration (coverage) of the surface defects in calculations of vacancies and adsorbed atoms and molecules.

The choice of the magnetic configuration only weakly affects the calculated surface relaxation and surface energies (Evarestov, et. al., 2005; Kotomin et al, 2008; Mastrikov et al., 2009). Relevant magnetic effects are sufficiently small (≈0.1eV) as do not affect noticeably relative stabilities of different surfaces; these values are much smaller than considered adsorption energies and vacancy formation energies. As for slabs the ferromagnetic (FM) configuration has the lowest energy, we performed all further plane-wave calculations with FM ordering of atomic spins.

The quality of plane-wave calculations can be illustrated by the results for the bulk properties (Evarestov, et. al., 2005; Mastrikov et al., 2009). In particular, for the low-temperature orthorhombic structure the A-type antiferromagnetic (A-AFM) configuration (in which spins point in the same direction within each [001] plane, but opposite in the neighbor planes) is the energetically most favorable one, in agreement with experiment. The lattice constant of both the cubic and orthorhombic phase exceeds the experimental value only by 0.5%. The calculated cohesive energy of 30.7 eV is also close to the experimental value (31 eV).

In our *ab initio* LCAO calculations we use DFT-HF (*i.e.*, density functional theory and Hartree-Fock) hybrid exchange-correlation functional which gave very good results for the electronic structure in our previous studies of both LMO and LSM (Evarestov et al., 2005; Piskunov et al., 2007). We employ here the hybrid B3LYP exchange-correlation functional (Becke, 1993). The simulations were carried out with the CRYSTAL06 computer code (Dovesi, et. al., 2007), employing BS of the atom-centered Gaussian-type functions. For Mn and O, all electrons are explicitly included into calculations. The inner core electrons of Sr and La are described by small-core Hay-Wadt effective pseudopotentials (Hay & Wadt, 1984) and by the nonrelativistic pseudopotential (Dolg et al., 1989), respectively. BSs for Sr and O in the form of 311d1G and 8–411d1G, respectively, were optimized by Piskunov et al., 2004. BS for Mn was taken from (Towler et al., 1994) in the form of 86–411d41G, BS for La is

provided in the CRYSTAL code's homepage (Dovesi, et. al., 2007) in form 311-31d3f1, to which we added an *f*-type polarization Gaussian function with exponent optimized in LMO (α=0.475). The reciprocal space integration was performed by sampling the Brillouin zone with the 4×4 Monkhorst-Pack mesh (Monkhorst & Pack, 1976). In our LCAO calculations, nine-layer symmetrical slabs (terminated on both sides by either [001] MnO_2 or La(Sr)O surfaces) were used. The calculations were carried out for cubic phases and for A-AFM magnetic ordering of spins on Mn atoms. All atoms have been allowed to relax to the minimum of the total energy. This approach was initially tested on bulk properties as well, the experimentally measured atomic, electronic, and low-temperature magnetic structure of pure LMO and LSM (x_b=1/8) were very well reproduced (Piskunov et al., 2007).

3. Thermodynamic analysis of surface stability

As was mentioned above, understanding of many surface related phenomena requires preliminary investigation of the relative stabilities of various crystalline surfaces. Usually (especially for high-temperature processes such as catalysis in electrochemical devices), determining the structure with the lowest internal energy is not sufficient. The internal energy characterizes only systems with a constant chemical composition, while atomic diffusion and atomic exchange between environment and surfaces occur at high temperatures. Thus, we have to take into account the exchange of atoms between the bulk crystal, its surface, and the gas phase, into our analysis of surface stability. Such processes are included into the Gibbs free energies at the thermodynamic level of description. Therefore, we have to calculate the surface Gibbs free energy (SGFE) Ω^i for the LMO and LSM surfaces of various orientations and terminations. The SGFE is a measure of the excess energy of a semi-infinite crystal in contact with matter reservoirs with respect to the bulk crystal (Bottin et al., 2003; Heifets et al., 2007a, 2007b; Johnston et al., 2004 ; Mastrikov et al., 2009; Padilla & Vanderbilt, 1997, 1998; Pikunov et al., 2008; Pojani et al., 1999; Reuter & Scheffler, 2001b, 2004). The SGFEs are functions of chemical potentials of different atomic species. The most stable surface has a structure, orientation and composition with the lowest SGFE among all possible surfaces.

3.1 Method of analysis for LMO surfaces

Introducing the chemical potentials μ_{La}, μ_{Mn}, and μ_O for the La, Mn, and O atomic species, respectively, the SGFE per unit cell area Ω^i corresponding to the *i* termination is defined as

$$\Omega^i = \frac{1}{2}[G^i_{slab} - N^i_{La}\mu_{La} - N^i_{Mn}\mu_{Mn} - N^i_O\mu_O], \quad (2)$$

where G^i_{slab} is the Gibbs free energy for the slab terminated by surface *i*, N^i_{La}, N^i_{Mn}, and N^i_O denote numbers of La, Mn, and O atoms in the slab. Here we assume that the slab is symmetrical and has the same orientation, composition, and structure on both sides. The SGFE per unit area is represented by

$$\omega^i = \frac{\Omega^i}{A} \quad (3)$$

The thermodynamic part of the description below follows the well known chemical thermodynamics formalism developed originally by Gibbs in 1875 (see Gibbs, 1948) for

perfect bulk and surfaces and extended by Wagner & Schottky, 1930 (also Wagner, 1936) for point defects.

The chemical potential μ_{LaMnO3} of LMO (in the considered orthorhombic or cubic phase) is equal to the sum of the chemical potentials of each atomic component in the LMO crystal:

$$\mu_{LaMnO3} = \mu_{La} + \mu_{Mn} + 3\mu_O \tag{4}$$

Owing to the requirement for the surface of each slab to be in equilibrium with the bulk LMO, the chemical potential is equal to the specific bulk crystal Gibbs free energy accordingly to

$$\mu_{LaMnO3} = g^{bulk}_{LaMnO3} \tag{5}$$

Eq. (4) imposes restrictions on μ_{La}, μ_{Mn}, and μ_O, leaving only two of them as independent variables. We use in following μ_O as one of the independent variables because we consider oxygen exchange between the $LaMnO_3$ crystal and gas phase and have to account for strong dependence of this chemical potential on T and pO_2. As another independent variable, we use μ_{Mn}. We will simplify the equation for the SGFE and eliminate the chemical potentials μ_{La} and μ_{LaMnO3} by substituting this expression for the LMO bulk chemical potential:

$$\Omega^i = \frac{1}{2}\left[G^i_{slab} - N^i_A g^{bulk}_{LaMnO3}\right] - \Gamma^i_{A,Mn}\mu_{Mn} - \Gamma^i_{A,O}\mu_O, \tag{6}$$

where $\Gamma^i_{A,a}$ are the Gibbs excesses in the i-terminated surface of components a with respect to the number of ions in A type sites (for ABO_3 perovskites) of the slabs (Gibbs,1948; Johnston et al., 2004) :

$$\Gamma^i_{A,a} = \frac{1}{2}\left(N^i_a - N^i_A \frac{N^{bulk}_a}{N^{bulk}_A}\right) \tag{7}$$

Here A type of sites are occupied solely by La atoms in LMO, so N_A=N_{La} for LMO. This will become somewhat more complicated in solid solutions such as LSM (see the next subsection). N^{bulk}_A is the number of A-sites in unit cell in the bulk. N^{bulk}_a is the number of a atoms in unit cell in the bulk.

The Gibbs free energies per unit cell for crystals and slabs are defined as

$$g_j = E_j + E^{vibr}_j - Ts_j + pv_j \tag{8}$$

where E_j is the static component of the crystal energy, E^{vibr}_j is the vibrational contribution to the crystal energy, v_j volume, and s_j entropy. All these values are given per formula unit in j-type (=La,Mn, LMO…) crystals. We can reasonably assume that the applied pressure is not higher than ~100 atm. in practical cases. The volume per lattice molecule in $LaMnO_3$ is ~64 $Å^3$. Then the largest pv_j term in Eq.(13) can be estimated as ~ 5 meV. This value is much smaller than the amount of uncertainty in our DFT computations and, therefore, can be safely neglected. As it is commonly practiced, we will neglect the very small vibration contributions to g_j, including contributions from zero-point oscillations to the vibrational part of the total energy. This rough estimate is usually valid, but can be broken if the studied material has soft modes. The same consideration is valid for slabs used in the present

simulations. While it might be important to check vibrational contributions in some cases, here we will neglect it. Besides, facilities in computer codes for calculations of vibrational spectra of crystals and slabs appeared only within a few last years and such calculations are still very demanding and practically possible only for relatively small unit cells. Therefore, we approximate the Gibbs free energies with the total energies obtained from DFT calculations:

$$g_j \approx E_j \tag{9}$$

Then, replacing the chemical potentials of La and Mn atoms by their deviations from chemical potentials in the most stable phases of respective elementary crystals,

$$\Delta\mu_{La} = \mu_{La} - g_{La}^{bulk} \approx \mu_{La} - E_{La}^{bulk} \tag{10}$$

and

$$\Delta\mu_{Mn} = \mu_{Mn} - g_{Mn}^{bulk} \approx \mu_{Mn} - E_{Mn}^{bulk} \tag{11}$$

and chemical potential of O atoms by its deviation from the energy of an oxygen atom in a free, isolated O_2 molecule ($E_{O_2}^{total}/2$),

$$\Delta\mu_O = \mu_O - \frac{E_{O_2}^{total}}{2} \tag{12}$$

we can determine the surface Gibbs free energy from

$$\Omega^i = \phi^i - \Gamma_{A,Mn}^i \Delta\mu_{Mn} - \Gamma_{A,O}^i \Delta\mu_O. \tag{13}$$

We can express the constant ϕ^i in Eq. (13) as

$$\begin{aligned} \phi^i &= \frac{1}{2}\left[G_{slab}^i - N_A^i g_{LaMnO3}^{bulk}\right] - \Gamma_{A,Mn}^i g_{Mn}^{bulk} - \frac{1}{2}\Gamma_{A,O}^i E_{O2} \approx \\ &\approx \frac{1}{2}\left[E_{slab}^i - N_A^i E_{LaMnO3}^{bulk}\right] - \Gamma_{A,Mn}^i E_{Mn}^{bulk} - \frac{1}{2}\Gamma_{A,O}^i E_{O2}\ , \end{aligned} \tag{14}$$

what resembles the expression for the Gibbs free energy of surface formation. Here E_{slab} stands for the total energy of a slab and replaces the Gibbs free energy of the slab.
The equilibrium condition (5) can be rewritten as

$$\Delta\mu_{La} + \Delta\mu_{Mn} + 3\Delta\mu_O = \Delta g_f^{bulk}(LaMnO_3) \tag{15}$$

where

$$\begin{aligned} \Delta g_f^{bulk}(LaMnO_3) &= g_{LaMnO3}^{bulk} - g_{La}^{bulk} - g_{Mn}^{bulk} - \frac{3}{2}E_{O2} \approx \\ &\approx E_{LaMnO3}^{bulk} - E_{La}^{bulk} - E_{Mn}^{bulk} - \frac{3}{2}E_{O2}\ . \end{aligned} \tag{16}$$

Here $\Delta g_f^{bulk}(LaMnO_3)$ has meaning of the Gibbs free energy of $LaMnO_3$ formation from La, Mn and O_2 in their standard states.
The range of values of the chemical potentials which consistent with existence and stability of the crystal (LMO here) itself is determined by the set of the following conditions. To prevent La and Mn metals from leaving LMO and forming precipitates, their chemical potentials must be lower in LMO than in corresponding bulk metals. These conditions mean:

$$\mu_{Mn} < g_{Mn}^{bulk} \tag{17}$$

and

$$\mu_{La} < g_{La}^{bulk} \tag{18}$$

Similarly, precipitation of oxides does not occur, if the chemical potentials of atoms in LMO are smaller than in the oxides:

$$2\mu_{La} + 3\mu_O < g_{La2O3}^{bulk} \tag{19}$$

$$\mu_{Mn} + \mu_O < g_{MnO}^{bulk} \tag{20}$$

$$3\mu_{Mn} + 4\mu_O < g_{Mn3O4}^{bulk} \tag{21}$$

$$2\mu_{Mn} + 3\mu_O < g_{Mn2O3}^{bulk} \tag{22}$$

and

$$\mu_{Mn} + 2\mu_O < g_{MnO2}^{bulk} \tag{23}$$

Exclusion of La chemical potential and expressing of these conditions through the deviations of the chemical potentials (10-12) transform the conditions to

$$\Delta\mu_{Mn} < 0 \tag{24}$$

$$\Delta\mu_{Mn} + 3\Delta\mu_O > \Delta g_f^{bulk}(LaMnO_3) \tag{25}$$

$$x\Delta\mu_{Mn} + y\Delta\mu_O < \Delta g_f^{bulk}(Mn_xO_y) \tag{26}$$

and

$$2\Delta\mu_{Mn} + 3\Delta\mu_O > 2\Delta g_f^{bulk}(LaMnO_3) - \Delta g_f^{bulk}(La_2O_3) \tag{27}$$

where the formation energies of oxides are defined by

$$\begin{aligned} \Delta g_f^{bulk}(M_xO_y) &= g_{MxOy}^{bulk} - x g_M^{bulk} - \frac{y}{2} E_{O2} \approx \\ &\approx E_{MxOy}^{bulk} - x E_M^{bulk} - \frac{y}{2} E_{O2}\,. \end{aligned} \tag{28}$$

Note, however, that sometimes compositions are fixed by bringing the multinary crystals into coexistence with less complex sub-phases.
If the SGFE becomes negative, surface formation becomes energetically favorable and the crystal will be destroyed. Therefore, the condition for sustaining a crystal structure is for SGFE to be positive for all potential surface terminations. Therefore, one more set of conditions on the chemical potentials of the crystal components can be written as

$$\Omega^i > 0 \tag{29}$$

where *i* corresponds to the surface with the lowest SGFE.

3.2 Method of analysis for LSM surfaces

In LSM we have to re-define the SGFEs, because there are now four components in this material (instead of three in LMO) with Sr atoms substituting a fraction of La atoms in the perovskite A sub-lattice. The SGFE definition for LSM can be written as

$$\Omega^i = \frac{1}{2}\left[G^i_{slab} - N^i_{La}\mu_{La} - N^i_{Sr}\mu_{Sr} - N^i_{Mn}\mu_{Mn} - N^i_O\mu_O\right] \tag{30a}$$

Let us denote concentration of Sr atoms in the bulk of LSM as

$$x_b = \frac{N^{bulk}_{Sr}}{N^{bulk}_{A}} \tag{30b}$$

where N^{bulk}_{Sr} is the average number of Sr atoms per crystal unit cell in the bulk. Then for LSM

$$N^{bulk}_{La} = (1 - x_b)N^{bulk}_{A} \tag{31}$$

becomes the average number of La atoms per LSM unit cell in the bulk.
The chemical potential of a LSM formula unit is

$$\mu_{LSM} = (1 - x_b)\mu_{La} + x_b\mu_{Sr} + \mu_{Mn} + 3\mu_O \tag{32}$$

Equilibrium between LSM surface and its bulk means that

$$\mu_{LSM} = g^{bulk}_{LSM} \tag{33}$$

We will continue using approximation (9) in the following, replacing the Gibbs free energies of bulk and slab unit cells by their total energies. The conditions (32, 33) impose restrictions on four chemical potentials of all LSM components and reduces the number of independent components to three. We have chosen to keep the chemical potentials of O, Mn and La as independent variables. Then the chemical potential of the Sr atom can be expressed as

$$\mu_{Sr} = \frac{1}{x_b}\left(E_{LSM} - (1 - x_b)\mu_{La} - \mu_{Mn} - 3\mu_O\right) \tag{34a}$$

and its deviation (analogous to eqs. (10-12) and keeping in mind approximation (9)) as

$$\Delta\mu_{Sr} = \mu_{Sr} - g_{Sr}^{bulk} \approx \mu_{Sr} - E_{Sr}^{bulk} \tag{34b}$$

The expressions for the excesses $\Gamma_{A,O}^{i}$ and $\Gamma_{A,Mn}^{i}$ do not change with respect to LMO. We still have to remember only that N_A does not coincide any more with N_{La} in LSM . N_A refers only to the number of A-sites in the perovskite unit cell, but not to the number of La atoms. Since we excluded chemical potential for Sr, only the excesses for La atoms will be required. For the calculation of excesses of La atoms we have to account for mixing of La and Sr atoms in A-site of the perovskite lattice. Using eqs.(7,31), the excess of La atoms for surface *i* can be expressed as:

$$\Gamma_{A,La}^{i} = \frac{1}{2}\left(N_{La}^{i} - \frac{N_{La}^{bulk}}{N_{A}^{bulk}} N_{A}^{i} \right) = \frac{1}{2}\left(N_{La}^{i} - (1-x_b) N_{A}^{i} \right) \tag{35}$$

Then SGFEs for LSM reads

$$\Omega^{i} = \phi^{i} - \Gamma_{A,La}^{i}\Delta\,\mu_{La} - \Gamma_{A,Mn}^{i}\Delta\mu_{Mn} - \Gamma_{A,O}^{i}\Delta\mu_{O} \tag{36}$$

where

$$\phi^{i} = \frac{1}{2}\left(G_{slab}^{i} - N_{A}^{i} E_{LSM}^{bulk} \right) - \Gamma_{A,La}^{i} E_{La}^{bulk} - \Gamma_{A,Mn}^{i} E_{Mn}^{bulk} - \Gamma_{A,O}^{i} \frac{E_{O_2}}{2} \tag{37}$$

The conditions of LSM crystal stability include the same bounds which work for LMO. However, we have to add conditions preventing precipitations of several new materials and express all conditions through three chemical potentials for La, Mn and O atoms. Precipitation of Mn, La, and Sr metals will be avoided if

$$\Delta\mu_{Mn} < 0 \tag{38}$$

$$\Delta\mu_{La} < 0 \tag{39}$$

and

$$(1-x_b)\Delta\mu_{La} + \Delta\mu_{Mn} + 3\Delta\mu_{O} > \Delta g_{f}^{bulk}(LSM) \tag{40}$$

where Gibbs free energy of LSM formation is

$$\Delta g_{f}^{bulk}(LSM) = E_{LSM}^{bulk} - x_b E_{Sr}^{bulk} - (1-x_b) E_{La}^{bulk} - E_{Mn}^{bulk} - \frac{3}{2} E_{O_2} \tag{41}$$

Precipitation of oxides is avoided, if

$$x\Delta\mu_{Mn} + y\Delta\mu_{O} < \Delta g_{f}^{bulk}(Mn_x O_y) \tag{42}$$

$$2\Delta\mu_{La} + 3\Delta\mu_{O} < \Delta g_{f}^{bulk}(La_2 O_3) \tag{43}$$

$$(1-x_b)\Delta\mu_{La} + \Delta\mu_{Mn} + (3-x_b)\Delta\mu_{O} > \Delta g_{f}^{bulk}(LSM) - x_b \Delta g_{f}^{bulk}(SrO) \tag{44}$$

where

$$\Delta g_f^{bulk}(SrO) = E_{SrO}^{bulk} - E_{Sr}^{bulk} - \frac{E_{O_2}}{2} \tag{45}$$

Similarly, precipitation of $LaMnO_3$ and $SrMnO_3$ perovskites will be prevented, if

$$\frac{1}{1-x_b}\Delta g_f^{bulk}(LSM) - \frac{x_b}{1-x_b}\Delta g_f^{bulk}(SrMnO_3) < \\ < \Delta\mu_{Mn} + \Delta\mu_{La} + 3\Delta\mu_O < \Delta g_f^{bulk}(LaMnO_3). \tag{46}$$

Here the Gibbs free energy of $SrMnO_3$ formation is defined as

$$\Delta g_f^{bulk}(SrMnO_3) = E_{SrMnO3}^{bulk} - E_{Sr}^{bulk} - E_{Mn}^{bulk} - \frac{3}{2}E_{O2}\ . \tag{47}$$

Lastly, spontaneous formation of surfaces does not occur, if condition (29) is satisfied as well.

3.3 Determination of the chemical potential of oxygen atom

As mentioned above, an exchange of O atoms between surfaces and environment occurs at all surfaces, especially at high temperatures. Moreover, such an exchange is a key factor in many electrochemical and catalytic processes. Therefore, oxygen in the studied crystal (for instance, LMO or LSM, in this Chapter) has to be considered in equilibrium with oxygen gas in atmosphere beyond the crystal surface. The equilibrium in exchange with O atoms means equality of oxygen chemical potentials in a crystal and in the atmosphere:

$$\mu_O = \frac{1}{2}\mu_{O2}^{gas} \tag{48}$$

Chemical potentials are hardly available experimentally. It is much more convenient to operate with gas temperatures and pressures determining the oxygen chemical potential. At the same time, the Gibbs free energies of crystals are insensitive to temperature and the pressure (within approximations accepted in our present description). Therefore, we can use the dependence of oxygen gas chemical potential μ_{O2}^{gas} to express the Gibbs free energies for surfaces through temperature and oxygen gas partial pressure.

Oxygen gas under the considered conditions can be treated (to a very good approximation) as an ideal gas. Therefore, dependence of its chemical potential from pressure can be expressed by the standard expression (as done by Johnston et al., 2004 and Reuter & Scheffler, 2001b)

$$\mu_{O2}^{gas}(T,p) = \mu_{O2}^{gas}(T,p^0) + kT\ln\left(\frac{p}{p^0}\right) \tag{49}$$

where k is the Boltzmann constant. Here p^0 is the reference pressure which we can take as the standard pressure (1 atm.). The temperature dependence of $\mu_{O2}^{gas}(T,p^0)$ includes contributions from molecular vibrations and rotations, as well as ideal-gas entropy at pressure p^0. We can evaluate the temperature dependence of $\mu_{O2}^{gas}(T,p^0)$ using experimental

data from the standard thermodynamic tables (Chase, 1998; Linstrom & Mallard, 2003), following Johnston et al., 2004 and Reuter & Scheffler, 2001b. These data are collected in Table 1. For this we define an isolated oxygen molecule E_{O2} as the reference state. Changes in the chemical potential for oxygen atom can be written as

$$\begin{aligned}\Delta\mu_O(T,p) &= \mu_O(T,p\ ) - \frac{1}{2}E_{O2} = \\ &= \frac{1}{2}\left\{\Delta G_{O2}^{gas}(T,p^0) + kT\ln\left(\frac{p}{p^0}\right)\right\} + \delta\mu_O^0\end{aligned} \tag{50}$$

Here $\Delta G_{O2}^{gas}(T,p^0)$ is the change in the oxygen gas Gibbs free energy at the pressure p^0 and temperature T with respect to its Gibbs free energy at T^0=298.15 K

$$\begin{aligned}\Delta G_{O2}^{gas}(T,p^0) &= G_{O2}^{gas}(T,p^0) - G_{O2}^{gas}(T^0,p^0) = \\ &= H_{O2}^{gas}(T,p^0) - H_{O2}^{gas}(T^0,p^0) - TS_{O2}^{gas}(T,p^0) + T^0 S_{O2}^{gas}(T^0,p^0)\end{aligned} \tag{51}$$

T, K	$\Delta G_{O2}^{gas}(T,p^0)$, eV	T, K	$\Delta G_{O2}^{gas}(T,p^0)$, eV
100	-0.07	1000	-1.10
200	-0.17	1100	-1.23
250	-0.22	1200	-1.36
298.15	-0.27	1300	-1.49
300	-0.27	1400	-1.62
400	-0.38	1500	-1.75
500	-0.50	1600	-1.88
600	-0.61	1700	-2.02
700	-0.73	1800	-2.16
800	-0.85	1900	-2.29
900	-0.97	2000	-2.43

Table 1. Variations in the Gibbs free energy for oxygen gas at standard pressure (p^0=1 atm.) with respect to its value at 0 K. Data are taken from thermodynamic tables (Chase, 1998; Linstrom & Mallard 2003).

The $\delta\mu_O^0$ in Eq. (50) is a correction which matches experimental data and the results of quantum-mechanical computations. This correction can be estimated from computations of metal oxides and metals, in a way similar to Johnston et al., 2004. Enthalpy of an M_xO_y oxide can be written as

$$h_{MxOy}^0 = xh_M^0 + \frac{y}{2}h_{O2}^0 + \Delta H_{f,MxOy}^0 \tag{52}$$

Here enthalpies of the oxide, h_{MxOy}^0, and of the metal, h_M^0, can be approximated by the total energies for these materials calculated at 0 K on the same grounds as for approximation

(9). The formation heat for La and Mn oxides under standard conditions can also be found in thermodynamic tables (Chase, 1998; Linstrom & Mallard, 2003). Equation (52) allows us to estimate the standard oxygen gas enthalpy. Since we define the total energy of an oxygen molecule as a zero for chemical potential and enthalpy calculations, the correction for the enthalpy could to be defined as

$$\delta h^0_{O2} = h^0_{O2} - E_{O2} \tag{53}$$

Using the experimental standard entropy for oxygen (Chase, 1998; Linstrom & Mallard, 2003) as $S^0_{O2} = 205.147$ J·mol^{-1}K^{-1}, the correction to the oxygen chemical potential can be calculated as

$$\begin{aligned}\delta\mu^0_O &= \frac{1}{2}(\delta h^0_{O2} - T^0 S^{gas}_{O2}(T^0, p^0)) \\ &= \frac{1}{y}(h^0_{M_xO_y} - x h^0_M - \Delta H^0_{f,M_xO_y}) - \frac{1}{2}(E_{O2} + T^0 S^{gas}_{O2}(T^0, p^0))\end{aligned} \tag{54}$$

3.4 Thermodynamic consideration of oxygen adsorption and vacancy formation

Let us consider formation of relevant oxygen species and point defects in the bulk and at the $LaMnO_3$ surface. We use the same approximation as in the previous sections: we neglect the changes of vibrational entropy in the solid, thus only states comprising gaseous O_2 exhibit the temperature-dependent Gibbs free energy contribution. In this approximation, differences between the Gibbs energies for bulk crystals or slabs (including defects and adsorbates) can be replaced with the differences in the total energy calculated from DFT, while variation of oxygen chemical potential for gaseous O_2 is taken from experimental data. The Gibbs free energy of reaction for removal of a neutral O atom (1/2 O_2) from the bulk (i.e. formation of one neutral V_O and allocation of the left-behind two electrons mainly on two nearest Mn) is defined as

$$\Delta g^{bulk}_f(LaMnO_3 : \mathrm{V_O}) = E^{bulk}\left(LaMnO_3 : \mathrm{V_O}\right) + \mu_O(T, p\mathrm{O}_2) - E^{bulk}_{LaMnO3} \tag{55}$$

where $E^{bulk}\left(LaMnO_3 : \mathrm{V_O}\right)$ is the total energy per bulk supercell with an oxygen vacancy. This definition can be re-written as

$$\Delta g^{bulk}_f\left(LaMnO_3 : \mathrm{V_O}\right) = \Delta E^{bulk}_f\left(LaMnO_3 : \mathrm{V_O}\right) + \Delta\mu_O(T, p\mathrm{O}_2) \tag{56}$$

where

$$\Delta E^{bulk}_f\left(LaMnO_3 : V_O\right) = E^{bulk}\left(LaMnO_3 : V_O\right) + \frac{1}{2}E_{O_2} - E^{bulk}_{LaMnO3} \tag{57}$$

is the formation energy of a neutral oxygen vacancy with respect to the calculated energy $\frac{1}{2}E_{O_2}$ for oxygen atom in the molecule. The variation of oxygen chemical potential

$\Delta\mu_O(T, pO_2)$ due to T, pO_2 is described by Eq. (50). Similarly, the vacancy formation energy for the surface vacancy can be presented as

$$\Delta g_f^{surf}\left(LaMnO_3:\mathrm{V_O}\right) = \Delta E_f^{surf}\left(LaMnO_3:\mathrm{V_O}\right) + \Delta\mu_{\mathrm{O}}(T, pO_2) \tag{58}$$

where

$$\Delta E_f^{surf}\left(LaMnO_3:\mathrm{V_O}\right) = \frac{1}{2}\left(E^{slab}\left(LaMnO_3:2V_O\right) + E_{O_2} - E_{LaMnO3}^{slab}\right) \tag{59}$$

Here we accounted for the fact that we use a symmetrical slab with an oxygen vacancy at each side of the slab. The total energy of such a slab is written as $E^{slab}\left(LaMnO_3:2V_O\right)$, because the slab has two vacancies. E_{LaMnO3}^{slab} is the total energy of the slab without defects. The Gibbs free energies of adsorption can be written in a similar way:

$$\Delta g_{ads}^{surf}\left(LaMnO_3:\ O_{ads}\right) = \Delta E_{ads}^{surf}\left(LaMnO_3:\ O_{ads}\right) - \Delta\mu_O \tag{60}$$

$$\Delta\ E_{ads}^{surf}\left(LaMnO_3:\ O_{ads}\right) = \frac{1}{2}\left(E^{slab}\left(LaMnO_3:2O_{ads}\right) - E_{O_2} - E_{LaMnO3}^{slab}\right) \tag{61}$$

and

$$\Delta g_{ads}^{surf}\left(LaMnO_3:\ O_{2,\,\mathrm{ads}}\right) = \Delta E_{ads}^{surf}\left(LaMnO_3:\ O_{2,\,\mathrm{ads}}\right) - \Delta\mu_{O2} \tag{62}$$

$$\Delta\ E_{ads}^{surf}\left(LaMnO_3:\ O_{2,\,\mathrm{ads}}\right) = \frac{1}{2}\left(E_{slab}\left(LaMnO_3:2O_{2,\,\mathrm{ads}}\right) - 2E_{O_2} - E_{LaMnO3}^{slab}\right) \tag{63}$$

Here $\mu_{O2}=2\mu_O$, and we have to take account for two adsorbed O or O_2 on the symmetrical slab. It is important to remember that the adsorption energy (60) for atomic O species is given relative to half an O_2 molecule, but not with respect to gaseous O atoms.
In the present Chapter we will describe the vacancy formation energies and the adsorption energies of O atoms and O_2 molecules obtained with plane wave BS and PW91 functional.

4. Results and discussions

4.1 Stability of LMO surface terminations: Plane-wave DFT simulations

Based on the results of plane-wave calculations and theoretical considerations described in Section 3, the phase diagrams characterizing stability of different LMO surfaces have been drawn in Figure 1. These diagrams were built for both low-temperature orthorhombic and high-temperature cubic phases. For O-terminated [011] and LaO+O [001] surfaces it was not possible to keep the cubic structure during lattice relaxation. Therefore, we used Ω^i values for the orthorhombic phase for both phase diagrams in Figure 1, as it was done, for instance, by Bottin et al., 2003. The calculated input data used for drawing this figure are collected in Tables 2 and 3. Optimized geometries for the slabs can be found in Mastrikov et al., 2009.
The surface stability regions in the diagrams are limited by the lines 2, 6 and 4. These lines correspond to boundaries where coexistence occurs of LMO with La_2O_3, MnO_2 and Mn_3O_4, respectively. Because of the DFT deficiencies in describing the relative energies for materials

surface		$\Gamma^i_{La,O}$	$\Gamma^i_{La,Mn}$	ϕ^i_{La} (eV/unit cell)	ϕ^i_{La} (J/m^2)
orientation	termination				
[001]	LaO	-1	-0.5	5.38 (5.42)	5.67 (5.70)
[001]	LaO+O	-0.875	-0.5	4.90	5.16
[001]	MnO_2	1	0.5	-3.02 (-2.93)	-3.18 (-3.08)
[001]	MnO_2+O	1.125	0.5	-3.16 (-3.53)	-3.33 (-3.72)
[110]	LaMnO	-1	0	6.13 (6.05)	4.56 (4.51)
[110]	O_2	1	0	-1.16 (-1.26)	-0.86 (-0.94)
[110]	O	0	0	1.09	0.81

Table 2. Parameters defining the surface Gibbs free energies Ω^i (Eq. 13) as function of O and Mn chemical potentials : excesses $\Gamma^i_{La,O}$ and $\Gamma^i_{La,Mn}$ of O and Mn atoms in the surfaces with respect to La atoms (7), and free energy of formation ϕ^i_{La} (14) at $\Delta\mu_O = \Delta\mu_{Mn} = 0$ eV for the $LaMnO_3$ surfaces under consideration. These results produced with plane wave BS and PW91 functional. Values of ϕ^i_{La} without brackets are for the orthorhombic phase, values in brackets are for the cubic phase. Reprinted with permission from Mastrikov et al., 2010 . Copyright 2010 American Chemical Society.

Crystal	Calculated $\delta\mu^0_O$	
	Plane wave BS + PW91	LCAO + B3LYP
La_2O_3	-0.41	-0.64
Mn_2O_3	-0.87	-0.53
MnO	-0.52	-0.59
MnO_2	-1.14	-0.09
Mn_3O_4	-0.90	-0.15
average	-0.77	-0.40

Table 3. The chemical potential correction (eV), Eq.(54), calculated for different oxides for both employed modeling techniques: (i) plane wave BS and PW91 functional and (ii) LCAO approach based on Gaussian-type atom-centered BS and hybrid B3LYP functional . The last line gives the average correction used in plotting the oxygen chemical potentials of the phase diagrams in Figures 1, 3, and 6.

with different degrees of oxidation, one should treat the obtained data with some precaution. Thus, we highlighted by solid lines the boundaries where metal oxides La_2O_3 and Mn_2O_3 with metals in oxidation state 3+ (lines 2 and 5) begin to precipitate in the perovskite. In these oxides, metal oxidation numbers coincide with the oxidation states for the same metals in $LaMnO_3$. Right hand side of the diagrams in Figure 1 contains a family of chemical potentials of O atoms (50) as functions of temperature and partial pressure of oxygen gas. This part of the figures allows us to translate easily-measurable external parameters (temperature and oxygen gas pressure) into oxygen chemical potential, which is one of the variables determining explicitly the SGFE. Using this part of the figures, we can relate points on the phase diagrams with the conditions under which experiments and/or industrial processes occur. To do this, one can just to draw a vertical line for a given temperature

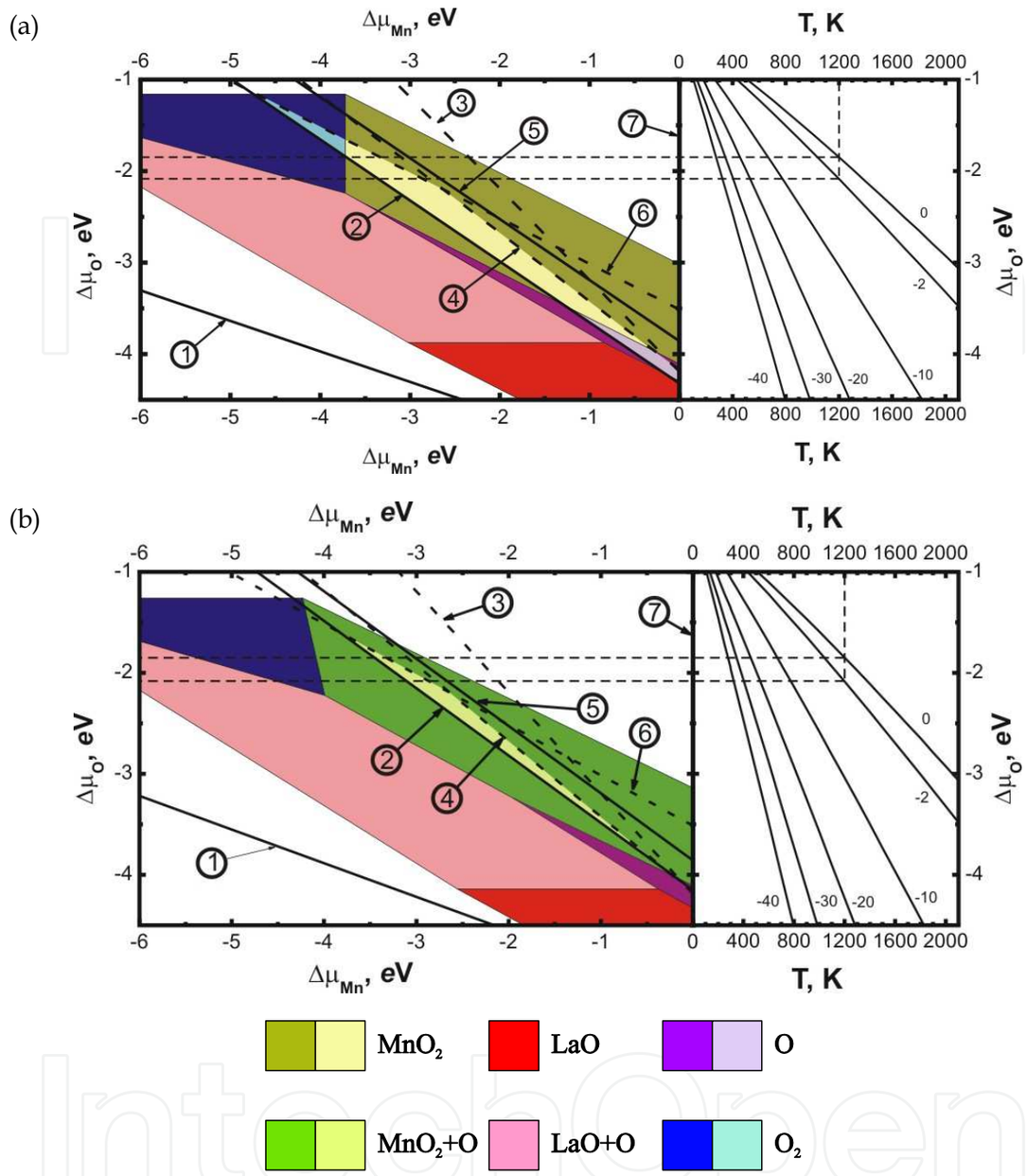

Fig. 1. Phase diagrams calculated with plane wave BS and PW91 GGA functional: The regions of stability of $LaMnO_3$ surfaces with different terminations (LaO- and MnO_2-terminated [001] surfaces without and with adsorbed O atom, O_2- and O-terminated [011] surfaces) for both orthorhombic (a) and cubic (b) phases as functions of manganese and oxygen atoms chemical potential variations. Parameters for all lines on the left side of the figures are collected in Table 2. The encircled numbers point to lines, where metals or their oxides begin to precipitate: (1) metal La, (2) La_2O_3, (3) MnO, (4) Mn_3O_4, (5) Mn_2O_3, (6) MnO_2, and (7) metal Mn. The right side of the figures contains a family of $\Delta\mu_O$ as functions of temperature at various oxygen gas pressures according to Eq. (50) and Table 1. The labels m on the lines specifies the pressure according to: $pO_2 = 10^m$ atm. Reprinted with permission from Mastrikov et al., 2010. Copyright 2010 American Chemical Society.

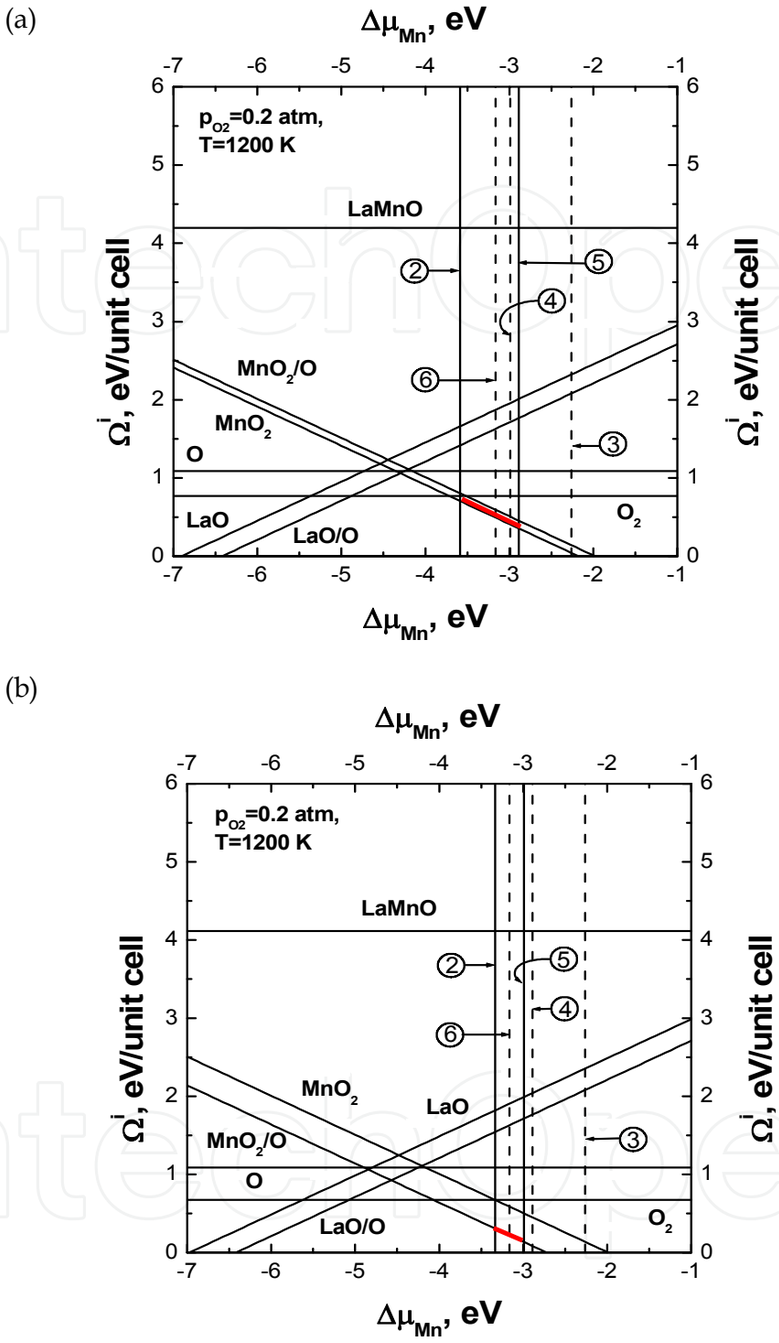

Fig. 2. Surface Gibbs Free Energies Ω^i for $LaMnO_3$ in (a) orthorhombic and (b) cubic phases as functions of $\Delta\mu_{Mn}$ at T = 1200 K and pO_2 = 0.2 atm Line numbers are the same as in Figure 4.1. The red lines indicate the most stable surface in the stability window between the precipitation lines for La_2O_3 and Mn_2O_3. Reprinted with permission from Mastrikov et al., 2010. Copyright 2010 American Chemical Society.

and its crossings with lines corresponding to different gas pressures creates a pressure scale for this particular temperature. This can replace the axis for oxygen chemical potential. Alternatively, moving along the lines for chemical potential at a particular gas pressure, we can study the phase behavior with temperature. Figure 1 shows such a consideration for T=1200 K which is a typical condition for SOFC operations. We marked on these phase diagrams the most important range of oxygen gas partial pressures (between pO_2 =0.2 atm. and 1 atm). Oxygen-rich conditions with a larger O chemical potential correspond to higher oxygen gas partial pressures and/or lower temperatures; in turn, oxygen-pure conditions with the lower O chemical potentials correspond to smaller oxygen gas partial pressures and/or higher temperatures.

Consistent positioning of these experimental curves with respect to our computed stability diagram requires also the correction described by Eq. (54). When drawing the right side of Figure 1, we used the correction of -0.77 eV (Table 3) calculated as average of a series of different oxides. It was calculated using the same set of oxides, which precipitation is considered in our plane-wave modeling. Both the values and the scattering (±0.37 eV) of calculated corrections are much larger than in similar studies (Heifets et al., 2007a, 2007b; Johnston et al., 2004; Reuter & Schefer, 2001a) for non-magnetic oxides (e.g. $SrTiO_3$).

Here we consider manganese oxides which are spin-polarized solids. Besides, we included several Mn oxides with various oxidation states. This is a typical situation where DFT calculations face well known problems. The scattering of the correction magnitudes provides an estimate of uncertainty in positioning of the chemical potentials for O atoms on the right side of the phase diagrams.

Figure 2 shows cross sections of the phase diagrams at T = 1200 K and pO_2 = 0.2 atm., i.e. in the range of typical SOFC operational conditions. Correspondingly, at the cross sections of the diagrams (Figure 2), the stability region lies between lines 2 and 6. This figure helps to clarify behavior of the SGFEs for surfaces with various terminations.

As it can be seen from Figures 1 and 2, under fuel cell operational conditions in both LMO phases the MnO_2-terminated [001] surface is the most stable one. In the orthorhombic phase it is the clean MnO_2-terminated surface, whereas in the high-temperature cubic phase the most stable surface contains adsorbed O atoms. This indicates that under identical conditions higher O adsorbate coverage is expected for the cubic LMO phase. Modeling with plane-wave BS and PW91 functional suggest that, when LMO crystal is heated, precipitation of La_2O_3 or Mn_3O_4 occurs, depending on chemical potentials variations during heating.

4.2 Stability of LMO surface terminations: LCAO simulations

Calculations performed within the LCAO approach combined with hybrid B3LYP functional were also employed in order to draw the phase diagram for stability of different LMO surface terminations (Figure 3). These calculations were carried out for a cubic phase and A-AFM magnetic ordering, where spins have the same orientations in the planes parallel to the surfaces of the slabs, but have opposite directions in neighbor planes. The comparison of stability shown in this figure includes only two primary candidates for the stable surfaces: LaO- and MnO_2-terminated (001) surfaces. The stability range is limited by lines 2, 3, and 5, which correspond to precipitation of La_2O_3, MnO, and Mn_2O_3. These are substantially different oxides than suggested above in computations performed with plane-wave BS and PW91 functional. Indeed, the gap between precipitation of La_2O_3 and Mn_2O_3 shifted down significantly. Now the boundary between stability regions for LaO- and

MnO_2-terminated surfaces crosses the gap where LMO is stable, while PW91-GGA calculations described above and by Mastrikov et al., 2009, 2010 suggested that only the MnO_2-terminated surface was stable. In calculations with hybrid B3LYP functional the MnO_2-terminated surface seems to be stable, up to SOFC operational temperatures (1200 K) under ambient oxygen gas partial pressures (pO_2=0.2 atm.). Above this temperature LaO-terminated surface gradually becomes more stable in the larger range in LMO crystal stability region until at ~1900 K it becomes the only stable surface. A precipitation of MnO or La_2O_3 has to occur while LMO crystal is heated.

Positioning the family of O atom chemical potential curves on the right side of Figure 3 was done in the same way as for Figure 1, but using LCAO calculations with hybrid B3LYP functional. The averaged correction $\delta\mu_O^0$ (54) in this case is noticeably smaller (-0.40 eV) than it was for PW91-GGA functional. However, deviations of this correction from its average value (±0.3 eV) is still large. This fact likely comes from the DFT difficulties, taking place even within hybrid functionals for spin-polarized systems. For diamagnetic systems, for instance $SrTiO_3$, such deviation drops down, from ~0.25 eV in LDA calculations (Johnston et al., 2004) to ~0.03 eV in calculations (Heifets et al., 2007b) with the hybrid functional.

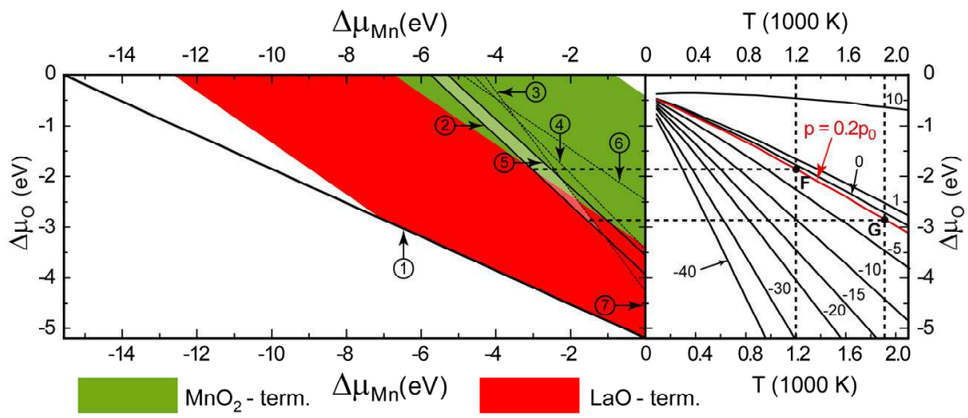

Fig. 3. Thermodynamic $LaMnO_3$ [001] surface stability diagram as a function of O and Mn chemical potentials. It compares stabilities of both LaO- and MnO_2-terminated [001] surfaces and accounts for precipitation conditions for (1) metal La, (2) La_2O_3, (3) MnO, (4) Mn_3O_4, (5) Mn_2O_3, (6) MnO_2, and (7) metal Mn, the same set as at Figures 1 and 2. The stable region is shown as lightened area between precipitation lines 2,3, and 5. The right side shows a family of oxygen chemical potentials under different conditions. The label m indicates the O_2 gas partial pressure: 10^m atm. Red line corresponds to oxygen partial pressure p=0.2p_0 as in the ambient atmosphere.

surface		$\Gamma^i_{La,O}$	$\Gamma^i_{La,Mn}$	ϕ^i_{La}	ϕ^i_{La}
orientation	termination			(eV/unit cell)	(J/m²)
[001]	LaO	-1	-0.5	6.32	6.46
[001]	MnO_2	1	0.5	-0.42	-0.43

Table 4. Parameters defining the surface Gibbs free energies Ω^i (Eq. 13) and used to build diagram in Figure 3. The same as Table 2, but for the cubic phase of LMO only and produced with LCAO approach and hybrid B3LYP functional.

4.3 Stability of surface terminations for LSM: LCAO simulations

Since the SGFEs for LSM surfaces depend now on three variables, it is a little more complicated to draw corresponding phase diagrams. Therefore, we have drawn only several sections for the most interesting parts of the phase diagram for bulk concentration of Sr atoms x_b= 1/8. Thus, Figure 4 shows the section of surface stability phase diagram under ambient oxygen gas partial pressure pO_2=0.2 atm. and three various temperatures: a) 300 K - room temperature (RT), b) 1100 K, which is approximately the SOFC operational temperature, and c) 1500 K, which is close to sintering temperatures. We compared several terminations of LSM (100) surfaces: MnO_2, $La_{1-x_s}Sr_{x_s}O$, in the last case concentrations of Sr atoms in the surface layer were varied: x_s= 0.25, 0.5, 0.75 and 1 (which simulates a segregation effect). Only three terminations appear at the shown sections: MnO_2, $La_{0.75}Sr_{0.25}O$, and SrO . Here we accounted for precipitation of metals (La, Mn, Sr), Mn_2O_3 and La_2O_3 oxides, and $LaMnO_3$ and $SrMnO_3$ perovskites. These sections of the surface phase diagram indicate that the LSM crystal can be stable only within a small quadrangle region in the presented sections. At low, room temperature two of considered terminations - MnO_2 and $La_{0.75}Sr_{0.25}O$ - are stable. At the higher temperatures $La_{0.75}Sr_{0.25}O$-terminated surface gradually occupies a larger portion of the stability region. Already at SOFC operational temperatures (T≈1100 K) this termination becomes stable in the entire stability region. Thus, Sr dopant atoms in LSM cause a relative stabilization of the

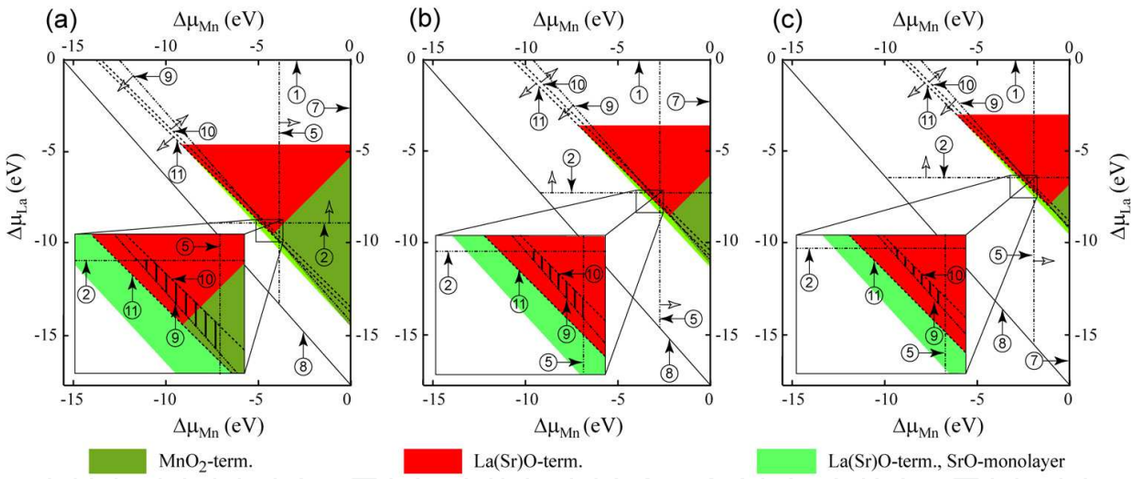

Fig. 4. Sections of surface stability diagram for LSM (001) surface structures for O_2 partial pressure p=0.2p_0 and temperatures of (a) 300 K (RT), (b) 1100 K (SOFC operational temperature), and (c) 1500 K (sintering temperature) (Piskunov et al., 2008). The region, where LSM (x_b= 1/8) is stable, is the shaded area between $LaMnO_3$, La_2O_3, Mn_2O_3, and SrO precipitation lines. The numbers from 1 to 11 in the circles indicate precipitation lines for (1) La, (2) La_2O_3, (3) MnO, (4) Mn_3O_4, (5) Mn_2O_3, (6) MnO_2, (7) Mn, (8) Sr, (9) SrO, (10) $LaMnO_3$, (11) $SrMnO_3$. (Some of the mentioned oxides are not considered in this Figure, but the numbering is designed to keep consistency of notations between figures.) Hollow arrows indicate the sides from respective precipitation lines where the precipitation occurs. Insets show magnified areas with the region of LSM stability (a shaded quadrangle). Reprinted with permission from Piskunov et al., 2008. Copyright 2008 American Physical Society.

$La_{1-x_s}Sr_{x_s}O$ - terminated surface with respect to the MnO_2-terminated surface. However, as soon as Sr concentration x_s at the $La_{1-x_s}Sr_{x_s}O$ -terminated surface becomes 0.5 or larger due to Sr segregation, such a surface becomes unstable.

For better understanding changes in the surface stability with temperature, we have drawn two additional cross-sections along the precipitation lines for SrO and $LaMnO_3$ at pO_2=0.2 atm. These cross-sections are presented in Figure 5. It can be seen here that upon heating the MnO_2-terminated surface leaves the stability region and becomes replaced by the $La_{0.75}Sr_{0.25}O$-terminated surface. As heating continues, precipitation of La_2O_3 or MnO begins. This is consistent with experimental observations by Kuo et al., 1989. A similar degradation process without Sr doping would require stronger overheating or very strongly reducing conditions. Detailed LCAO hybrid functional calculations of oxygen atom adsorption are necessary (see preliminary results in Piskunov et al, 2011), in order to check PW91-GGA prediction (discussed in previous subsection) that the MnO_2-terminated surface is stabilized by adsorbed oxygen atoms.

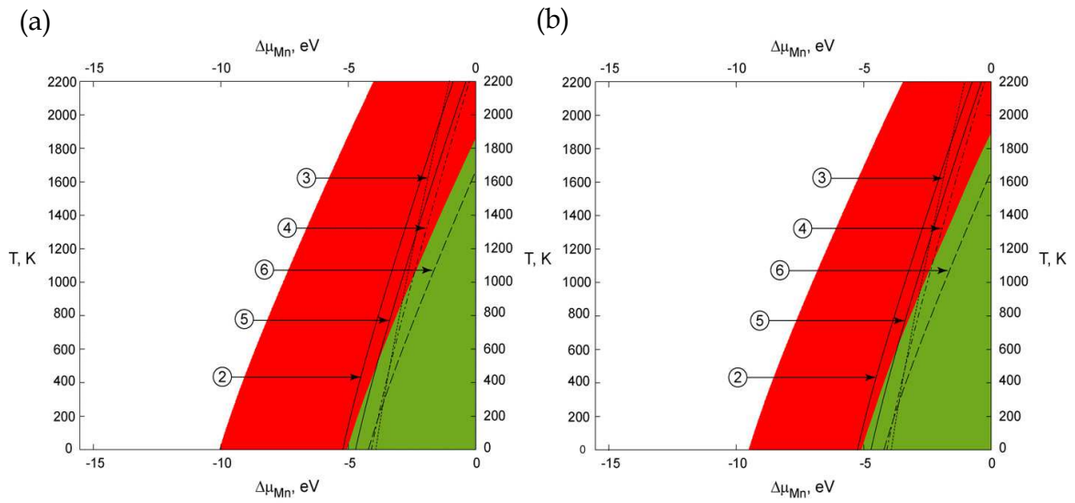

Fig. 5. LCAO calculated cross-sections of surface stability diagram for LSM (001) surface structures along (a) SrO and (b) $LaMnO_3$ precipitation lines for O_2 partial pressure p=0.2p_0 . Meaning of colors (terminations) and numbers (correspond to precipitation lines) are the same as in Figure 4.

4.4 Oxygen adsorption and vacancy formation in LMO

As shown above, the MnO_2-terminated (001) surface of $LaMnO_3$ appears to be the most stable one. Therefore, we optimized the atomic structure of surface oxygen vacancies, as well as O atoms and O_2 molecules adsorbed at different sites on this surface. For a comparison we also optimized the structure of oxygen vacancies in the $LaMnO_3$ bulk and at the LaO-terminated [001] surface. These simulations were performed using plane wave BS and PW91 functional. Details of the atomic position optimization are described by Mastrikov et al., 2010. In this Chapter, we limit our discussion only to the energies of different adsorbed species and vacancies and thermodynamic consideration of the relevant processes. Note that some adsorbed species have tilted geometry. For example, the lowest energy for the adsorbed O_2 molecule on MnO_2-terminated surface is atop of Mn ion with the angle between O-O bond and Mn-O direction being ~50^o .

The adsorption energies for O atoms ($\Delta E_{ads}^{surf}\left(LaMnO_3 : O_{ads}\right)$ and O_2 molecules ($\Delta E_{ads}^{surf}\left(LaMnO_3 : O_{2,\,ads}\right)$), as well as the surface and bulk formation energies ($\Delta E_f^{surf}(LaMnO_3 :\ V_O)$ and $\Delta E_f^{bulk}(LaMnO_3 :\ V_O)$) for oxygen vacancies are collected in Table 5. For a classification of different molecular oxygen species we considered atomic charges and the O-O bond length. The data in Table 5 suggest that atomic adsorption of O atoms is energetically more preferable than adsorption of O_2 molecule. In both cases the best adsorption site for both O atom and O_2 molecule on MnO_2-terminated surface is on top of surface Mn ion. Oxygen vacancies have smaller formation energy on MnO_2-terminated surface than in the bulk suggesting vacancy segregation towards this surface. In contrary, much more energy is required to create an oxygen vacancy on LaO-terminated surface.

Label of configuration	$-E_f$ or E_{ads}, eV	Charge, e_0	O-O distance, Å	"chemical assignment"
		0.	1.30	gaseous O_2
I	-1.1[a)]	-0.42	1.36	tilted superoxide atop one Mn^{surf}
II	-0.9[a)]	-0.65	1.42	horizontal peroxide atop one Mn^{surf}
III	-0.9[a)]	-0.69	1.41	horiz. peroxide atop O^{surf}
VII	-0.5 [a)]	-0.84	1.62	TS of dissociation without $V_{\ddot{O}}$, atop O^{surf} and bridging two Mn^{surf}
IV	-2.8[a)]	-1.19	1.50	tilted peroxide in $V_{\ddot{O}}$
V	-2.4[a)]	-1.25	1.50	"vertical peroxide" in $V_{\ddot{O}}$
V	+0.9[b)]	-1.25	1.50	TS of O^- diffusion along surface
VI	-1.1[b)]	-0.62		O^- adsorbed atop Mn
VI′	-1.8 [b)]			O^- adsorbed next to a surface vacancy
VIII	-3.3[b)]	-1.19		O ion in MnO_2[001] surface layer
IX	-4.3[b)]	-1.25		bulk O ion
X	-5.1[b)]	-1.32		O ion in LaO[001] surface layer

Table 5. Bond lengths, Bader charges and "chemical assignment" of the different oxygen species. Experimental O-O bond lengths (NIST, 2010) for comparison: gaseous O_2 1.21 Å, hydrogen superoxide radical HO_2 1.33 Å, hydrogen peroxide H_2O_2 1.48 Å. TS = transition state. Energies (compare Figure 4.6; for adsorbate coverage of 12.5 %): [a)] relative to gaseous O_2 in triplet state over defect-free surface, [b)] relative to half a gaseous O_2 over defect-free surface.

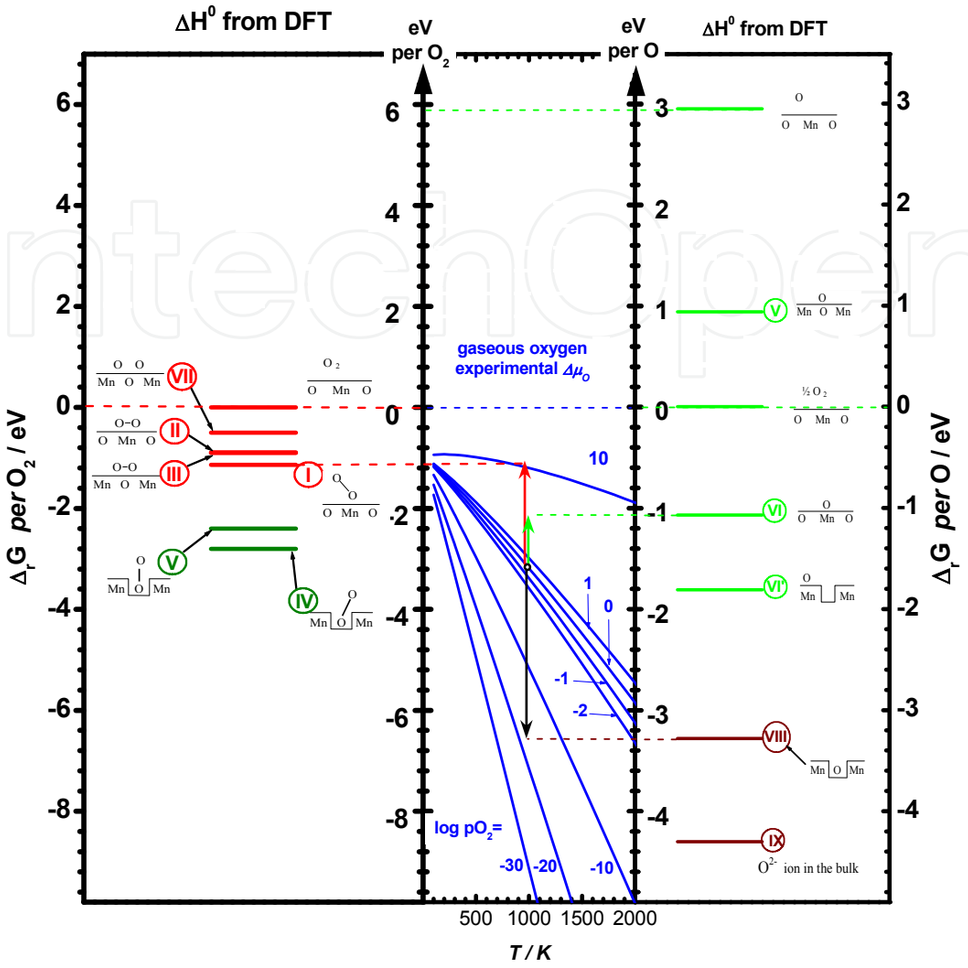

Fig. 6. Spectrum of possible "one-particle" states, where "particles" are O atoms (right panel) and O_2 molecules (left panel). Each level in these panels corresponds to relative energies (ΔE_r) of different molecular and atomic species occurring during oxygen incorporation reaction on the MnO_2[001]-terminated surface of $LaMnO_3$, cf. Table 5. The axes on the left and right give the energy ΔE_r relative to resting O_2 molecule away from the surface (on the left) or an atom in such O_2 molecule (on the right). In the ground state of the crystal all lattice sites in crystal bulk (states X) and I surface (states VIII) are occupied (red levels) and the rest of the "one-particle" states vacant. The numbers at levels correspond to the numbers assigned to respective states in Table 5. The highest level on the right panel corresponds to a free (not in a molecule) O atom away from the crystal. The central panel shows the experimental T- and pO_2-dependence of the Gibbs energy of gaseous O_2 (Table 1 and Eq.(50)), its energy scale refers to an O_2 molecule on the left and to an O atom in an O_2 molecule on the right. The labels m on the lines represent the pressure: $pO_2=10^m$ atm. The arrows indicate various Gibbs reaction energies due to moving of a "particle" between crystal and gas: red = formation of adsorbed superoxide O_2^- on defect-free surface; green = formation of adsorbed O^- atop Mn on defect-free surface; black = incorporation of oxygen into a surface oxygen vacancy.

The collected energies allow us to draw the diagram shown in Figure 6. This diagram is based on a standard model of "non-interacting particles", where "particles" are O atoms and O_2 molecules in different positions. The energy levels drawn at the side panels represent single- particle energies corresponding to bringing a particle to a given position at the surface or in the bulk. The left hand panel refers to bringing a free gas-phase O_2 molecule to the crystal surface. Similarly, the right hand panel refers to taking an O atom from a free O_2 molecule and placing it on the crystal surface. These processes include also placing of an atom or a molecule into surface vacancies: this is a process inverse to the formation of a vacancy. Therefore, to place the corresponding energy level (at right hand panel), one has to use the vacancy formation energy with the opposite sign. A similar logic was applied in placing the energy level for bringing an oxygen atom into vacancy in the bulk. Such an O atom in a vacancy becomes actually a regular O atom in the crystal lattice (wherever, in the bulk or in the surface). Therefore, the energies of such states can be considered as those for an O atom in the bulk or on the surface. In the ground state of the crystal all lattice sites (states VIII, IX and X) are occupied and all other states vacant.

The variation of the oxygen chemical potential is drawn in the central panel as a function of temperature for several gas partial pressures. These curves are drawn in the same way as similar lines on the right hand side in Figure 1, including the offset defined by Eq. (54). Because the energy scale at the left panel is twice as large as at the right panel, the same curves represent variations either in the chemical potentials for an O_2 molecule, if they are referred to the left panel, or for O atom, if they are referred to the right one. In such an arrangement, the diagram in Figure 6 can be used to represent the Gibbs energies for reactions of exchange with O atoms or O_2 molecules between oxygen gas and both crystal bulk and surfaces. For example, red arrow represents an adsorption of an O_2 molecule atop surface Mn ion in the tilted position (configuration I) from oxygen gas under partial pressure pO_2=1 atm. and T=1000 K. The Gibbs free energy of corresponding reaction can be obtained by subtracting the energy of the initial state from that of the final state. For the reaction described by the red arrow this energy indeed corresponds to the adsorption energy for O_2 molecule. Similarly, the green arrow describes the adsorption of O atom atop Mn ion in MnO_2 –terminated surface. Lastly, the black arrow describes incorporation of an O atom into a surface oxygen vacancy. In the latter case, an arrow with opposite direction corresponds to the formation of a surface oxygen vacancy, as it can be confirmed by a comparison with Eqs. (60, 61).

The diagram in Figure 6 is very suitable way of a graphical representation of the exchange between a gas and a crystal with various species and the analysis of corresponding processes. For a given temperature and oxygen partial pressure this diagram allows one to read the Gibbs reaction energy of a process and thus to obtain its mass action constant. As an example, let us discuss some processes under typical fuel cell conditions of T = 1000 K and pO_2 = 1 atm. The formation of molecular adsorbates (superoxide I = red arrow, and peroxide II) is endergonic by $\Delta_r G \approx +2$ eV per O_2 since the entropy loss overcompensates the electronic energy gain. Even the formation of adsorbed atomic O^- (species VI, green arrow) is still slightly endergonic, by $\Delta_r G \approx +0.5$ eV per O, what leads the low adsorbate coverage under SOFC conditions. Only the oxygen incorporation into a surface vacancy (black arrow) is strongly exergonic, by $\Delta_r G \approx -1.7$ eV per O (i.e. the inverse process, surface oxygen vacancy formation, is endergonic by +1.7 eV). Also, changes in temperature and/or partial pressure can change the sign of the reaction energy. To give an example: while oxygen atom adsorption is exothermic here, it changes from exergonic at low temperatures and/or high partial pressures to endergonic at higher temperatures and/or lower pressures.

5. Conclusions and perspectives

In this Chapter, combining *ab initio* calculations of the atomic and electronic structure with chemical thermodynamics, we have described how to predict surface stabilities with different orientations and terminations for ABO_3 perovskite materials and solid solutions. We considered also adsorption and formation of vacancies in the bulk and at the surfaces. The input data for such thermodynamic analyses are available from standard DFT calculations. We neglected vibrational contributions to the Gibbs free energies in present simulations, since there are good arguments that these contributions are quite small. However, the latest versions of the computer codes used here (VASP and CRYSTAL) are capable to perform the calculations of phonon spectra, which can be used to include vibration contributions into thermodynamic potentials. Despite currently such surface phonon calculations are computationally very expensive, with development of new algorithms and faster computers such analysis in near future could become a routine practice.

We have applied the described techniques to experimentally well studied SOFC cathode materials (LMO and LSM). The energies calculated by DFT techniques allow us to draw the surface stability diagrams showing that under the SOFC operational conditions MnO_2-terminated surface of defect/dopant-free LMO is the most stable. The MnO_2-terminated surface with adsorbed O atoms becomes more stable in a cubic phase of LMO. (The analysis based on results of calculations with hybrid functional gives higher precision of the obtained diagrams). Introduction of Sr dopant into LMO leads to a significant decrease of stability of MnO_2-terminated surface with respect to stability of Sr-containing $La_{1-x_s}Sr_{x_s}O$-terminated surface. At elevated temperatures only the latter one can be found within an entire region of LSM stability which definitely should affect the LSM cathode performance due to our prediction that oxygen vacancies easily segregate from LMO bulk towards MnO_2-terminated surface but not to the LaO-terminated one (Mastrikov et al, 2010).

Thermodynamic consideration of oxygen adsorption and formation of surface vacancies allowed us to move beyond the usual analysis of purely DFT electronic energy differences in these processes at zero K and to describe changes in the Gibbs free energies under realistic environmental conditions (high temperature and partial pressure of oxygen gas). In particular, we have shown that an oxygen adsorption from the gas phase is exergonic at low temperatures, but becomes endergonic at SOFC operational temperatures. Consideration of the energy differences between O atoms and O_2 molecules in the gas phase and at surfaces makes it possible to determine theoretically preferred adsorption sites, adsorption energies and formation energies for vacancies (e.g. Kotomin et al., 2008, Mastrikov et al., 2010, and Piskunov et al, 2011). Thus the obtained data can be used for analysis of the kinetics of chemical reactions and investigation of their mechanisms. For example, we performed such an analysis (Mastrikov et al., 2010) in the study of oxygen reduction and incorporation into the LMO surfaces.

Note also that under realistic experimental conditions in a multinary crystal typically only one component is reversibly exchangeable so that only one chemical potential can be varied in-situ. Typically the others are varied under preparation conditions, and then so-established sublattice stoichiometry is frozen under experimental conditions. This complex interplay of in-situ and ex-situ parameters has been discussed by Maier, 2003.

Various questions, where thermodynamic approach is necessary, are still open. One example is Sr segregation towards LSM surfaces which was experimentally observed e.g. by

Fister et al., 2008 and Herger et al., 2008. In the study by Herger et al., 2008, the Sr segregation energy was estimated to be ~0.16 eV while preliminary theoretical estimate gave the segregation energy ~0.54 eV (Piskunov et al., 2008). Another question is, how vacancy formation and oxygen adsorption energies depend on surface Sr concentration. Lastly, our present simplified simulations assume that LMO and LSM have large flat surfaces. However, one can expect in reality much more rough surface structure containing many facets and steps. This is important also because SOFC cathode materials are polycrystalline. Therefore, there is a necessity to check, which kinds of steps and facets are the most stable ones and likely to exist at LMO and LSM surfaces and how their presence affects adsorption of oxygen atoms and molecules, vacancy formation and reactions occurring at the surfaces.

6. Acknowledgements

EH is indebted to the Max Planck Institute for financial support through the honorary contract. EK, YM thank the EC FP7 NASA-OTM project (grant agreement N 228701) for partial financial support. S.P. is thankful for the financial support through the ESF project Nr. 2009/0216/1DP/1.1.1.2.0/09/APIA/VIAA/044. This study was supported by a grant of computer time at the EMS Laboratory at PNNL (Project No 42498). Authors are greatly indebted to R. Merkle, J. Fleig, R.A. Evarestov, D. Gryaznov, C. Noguera, and M. W. Finnis for many stimulating discussions.

7. References

Becke, A. D. (1993). A new mixing of Hartree–Fock and local density–functional theories. *Journal Chemical Physics*, Vol.98, No.2, (January 1993), pp. 1372-1377, ISSN: 1089-7690

Bloechl, P. E. (1994). *Physical Review B*, Vol. 50, No.24 , (December 1994), pp.17953- 17979, ISSN: 1550-235X

Bottin, F.; Finocchi, F. & Noguera, C. (2003). Stability and electronic structure of the (1×1) $SrTiO_3$(110) polar surfaces by first-principles calculations. *Physical Review B*, Vol.68, No.3, (July 2003), a.035418 , ISSN: 1550-235X

Chase, M.W. (1998). *NIST-JANAF Thermochemical Tables,* American Chemical Society, Washington, DC, USA, ISNB: 1563968312

Coey, J. M. D.; Viret M. & von Molnár, S. (1999). Mixed-valence manganites. *Advances in Physics*, Vol.48, No.2, (November 2010), pp. 167–293, ISSN 1460-6976

Dolg, M.; Stoll, H.; Savin, A. & Preuss, H. (1989). Energy-adjusted pseudopotentials for the rare earth elements. *Theoretica Chimica Acta*, Vol.75, No.3, (December 1989), pp. 173-194, ISSN: 1432-2234

Dovesi R.; Saunders, V.R.; Roetti, C.; Orlando, R.; Zicovich-Wilson, C. M.; Pascale, F.; Civalleri, B.; Doll, K.; Harrison, N.M.; Bush, I.J.; D'Arco, Ph. & M. Llunell (2007) *CRYSTAL06 User's Manual,* University of Torino, Torino, Italy, Retrieved from http://www.crystal.unito.it/

Evarestov, R. A.; Kotomin, E. A.; Mastrikov, Yu.; Gryaznov, D.; Heifets, E. & Maier, J. (2005). Comparative density-functional LCAO and plane-wave calculations of $LaMnO_3$ surfaces. *Physical Review B*, Vol. 72, No.21 , (December 2005), a. 214411, ISSN: 1550-235X

Fister, T.T.; Fong, D.D.; Eastman, J.A.; Baldo, P.M.; Highland, M.J.; Fuoss, P.H.; Balasubramaniam, K. R.; Meador, J. C. & Salvador, P. A. (2008). *In situ* characterization of strontium surface segregation in epitaxial $La_{0.7}Sr_{0.3}MnO_3$ thin films as a function of oxygen partial pressure *Applied Physics Letters*, Vol. 93, No. 15, (October 2008), a. 151904, ISSN 1077-3118

Fleig J.; Kreuer, K.D. & Maier, J. (2003). Ceramic Fuel Cells, In: *Handbook of Advanced Ceramics: Processing and Their Applications, Vol. II*, S. Somiya, (ed.), F. Aldinger (Ed.), R. M. Spriggs (Ed.), K. Uchino (Ed.), K. Koumoto (Ed.), M. Kaneno (Ed.), pp. 59–105, Elsevier, ISBN 978-0-12-654640-8, Amsterdam, Netherlands.

Gibbs J.W. (1948). *Collected Works*, Yale University Press, New Haven, USA

Haghiri-Gosnet, A. & Renard, J. (2003). CMR manganites: physics, thin films and devices *Journal of Physics D*, Vol.36, No.8, (April 2003), pp. R127-R150, ISSN 1361-6463

Hay P. J. & Wadt, W. R. (1985). Ab initio effective core potentials for molecular calculations. Potentials for K to Au including the outermost core. *Journal Chemical Physics*, Vol.82, No.1, (January 1985), pp. 299-310 , ISSN: 1089-7690

Heifets E.; Ho, J. & Merinov, B. (2007a). Density functional simulation of the BaZrO3 (011) surface structure. *Physical Review B*, Vol. 75, No.15, (April 2007) a. 155431, ISSN: 1550-235X

Heifets, E.; Piskunov, S.; Kotomin, E. A.; Zhukovskii, Y. F. & Ellis, D., (2007b). Electronic structure and thermodynamic stability of double-layered $SrTiO_3$ (001) surfaces: *Ab initio* simulations. *Physical Review B,* Vol.75, No.11, (March 2007), a. 115417 , ISSN: 1550-235X

Herger, R.; Willmott, P. R.; Schlepütz, C. M.; Björck, M.; Pauli, S. A.; Martoccia, D.; Patterson, B. D.; Kumah, D.; Clarke, R.; Yacoby, Y. & Döbeli, M. (2008). Structure determination of monolayer-by-monolayer grown $La_{1-x}Sr_xMnO_3$ thin films and the onset of magnetoresistance. *Physical Review B*, Vol.77, No.8 , (February 2008), a. 085401, ISSN: 1550-235X

Johnston, K.; Castell, M. R.; Paxton, A. T. & Finnis, M. W. (2004). $SrTiO_3$(001)(2×1) First-principles calculations of surface energy and reconstructions: atomic structure compared with scanning tunneling microscopy images. *Physical Review B*, Vol.70, No.8, (August 2004), a. 085415 ISSN: 1550-235X

Kotomin, E.A.; Mastrikov, Yu.; Heifets, E. & Maier, J. (2008). Adsorption of atomic and molecular oxygen on the $LaMnO_3$ surfaces: *ab initio* supercell calculations and thermodynamics, *Physical Chemistry Chemical Physics*, Vol. 10, No. 7, (June 2008), pp. 4644-4649, ISSN: 1463-9084

Kresse, G. & Hafner, J. (1993). Ab initio molecular dynamics for liquid metals. *Physical Review B*, Vol. 47, No.1 , (January 1993), pp. 558-561,

Kresse, G. & Furthmüller, J. (1996). *Physical Review B*, Vol. 54, No.16 , (October 1996) , pp.11169-11186, ISSN: 1550-235X

Kresse, G. & Joubert,D. (1999). From ultrasoft pseudopotentials to the projector augmented-wave method. *Physical Review B*, Vol. 59, No.3 , (January 1999), pp. 1758-1775, ISSN: 1550-235X

Kresse, G.; Marsman, M. & Furthmüller, J. (2011) *VASP, the Guide*, University of Vienna, Austria, Available from http://cms.mpi.univie.ac.at/vasp/vasp/vasp.html

Kuo J. H.; Anderson, H. U. & Sparlin D. M. (1989). Oxidation-reduction behavior of undoped and Sr-doped $LaMnO_3$ nonstoichiometry and defect structure. *Journal of Solid State Chemistry*, Vol.83, No.1, (November 1989), pp. 52-60, ISSN: 0022-4596

Linstrom, P.J.(ed.) & Mallard, W.G.(ed.) (2003). *NIST Chemistry WebBook, NIST Standard Reference Database No. 69*, National Institute of Standards and Technology, Gaithersburg, MD, USA, Available from http://webbook.nist.gov/chemistry/

Maier J. (2003) Complex oxides: high temperature defect chemistry vs low temperature defect chemistry. *Physical Chemistry Chemical Physics*, Vol. 5, No.11, (April 2003), pp. 2164-2173, ISSN: 1463-9084

Mastrikov, Yu. A.; Heifets, E.; Kotomin, E. A. & Maier, J. (2009). Atomic, electronic and thermodynamic properties of cubic and orthorhombic $LaMnO_3$ surfaces. *Surface Science*, Vol. 603, No.2, (January 2009), pp. 326-335 , ISSN: 00396028

Mastrikov, Yu. A.; Merkle, R.; Heifets, E.; Kotomin, E. A. & Maier, J. (2010). Pathways for Oxygen Incorporation in Mixed Conducting Perovskites: A DFT-Based Mechanistic Analysis for (La, Sr)$MnO_{3-\delta}$. *Journal Physical Chemistry C,* Vol.114, No. 7, (July 2010), pp. 3017–3027, ISSN: 1932-7455

Monkhorst, H. J.& Pack, J. D. (1976). Special points for Brillouin-zone integrations. *Physical Review B*, Vol.13, No.12, (June 1976), pp. 5188-5192, ISSN: 1550-235X

NIST (2010). *NIST computational chemistry comparison and benchmark database*, NIST, Gaithersburg, Maryland, USA, Available from http://cccbdb.nist.gov/

Padilla J. & Vanderbilt, D. (1997). Ab initio study of $BaTiO_3$ surfaces. *Physical Review B*, Vol.56, No. 3, (July 1997), pp. 1625-1631, ISSN: 1550-235X

Padilla J. & Vanderbilt, D. (1998). Ab initio study of $SrTiO_3$ surfaces *Surface Science*, Vol.418, No.1, (November 1998), pp. 64-70 , ISSN: 00396028

Perdew, J. P.; Chevary, J. A.; Vosko, S. H.; Jackson, K. A.; Pederson, M. R.; Singh, D. J. & Fiolhais, C. (1992). Atoms, molecules, solids, and surfaces: Applications of the generalized gradient approximation for exchange and correlation. *Physical Review B*, Vol.46, No.11 , (September 1992), pp. 6671-6687, ISSN: 1550-235X

Piskunov, S.; Heifets, E.; Eglitis, R. I. & Borstel, G. (2004). Bulk properties and electronic structure of $SrTiO_3$, $BaTiO_3$, $PbTiO_3$ perovskites: an ab initio HF/DFT study. *Computational Materials Science*, Vol. 29, No.2, (February 2004), pp. 165-178, ISSN: 0927-0256

Piskunov, S.; Spohr, E.; Jacob, T.; Kotomin, E.A. & Ellis D. (2007). Electronic and magnetic structure of $La_{0.875}Sr_{0.125}MnO_3$ calculated by means of hybrid density-functional theory. *Physical Review B*, Vol. 76, No.1 , (July 2007), a. 012410, ISSN: 1550-235X

Piskunov, S.; Heifets, E.; Jacob, T.; Kotomin, E. A.; Ellis, D. E. & Spohr, E. (2008). Electronic structure and thermodynamic stability of $LaMnO_3$ and $La_{1-x}Sr_xMnO_3$ (001) surfaces: Ab initio calculations. *Physical Review B*, Vol.78, No.12, (September 2008), a. 121406, ISSN: 1550-235X

Piskunov, S.; Jacob, T. & Spohr, E (2011). Oxygen adsorption at $La_{1-x}Sr_xMnO_3$ (001) surfaces: Predictions from first principles. *Physical Review B*, Vol.83, No.7, (February 2011), a. 073402, ISSN: 1550-235X

Piskunov, S.; Jacob, T. & Spohr E. (2011) Oxygen adsorption at (La,Sr)MnO3 (001) surfaces: Predictions from first principles. *Physical Review B,* Vol. 85, No 7, (February 2011), pp. 073402 (1-4), ISSN: 1550-235X

Pojani, A.; Finocchi, F. & Noguerra, C. (1999). Polarity on the $SrTiO_3$ (111) and (110) surfaces. *Surface Science*, Vol.442, No.2, (November 1999), pp. 179 -198, ISSN: 00396028

Reuter, K. & Scheffler, M. (2001a). Stability and electronic structure of the (1×1) $SrTiO_3$(110) polar surfaces by first-principles calculations. *Surface Science,* Vol. 490, No. 1-2, (September 2001), pp. 20-28, ISSN: 00396028

Reuter, K. & Scheffler, M. (2001b). Composition, structure, and stability of RuO_2(110) as a function of oxygen pressure. *Physical Review B*, Vol.65, No. 3, (December 2001), a. 035406 , ISSN: 1550-235X

Reuter K. & Scheffler, M. (2004). Oxide formation at the surface of late 4d transition metals: insights from first-principles atomistic thermodynamics. *Applied Physics A*, Vol.78, No.6, (February 2004), pp. 793-798, ISSN: 1432-0630

Towler, M. D.; Allan, N. L.; Harrison, N. M.; Saunders, V. R.; Mackrodt, W. C. & Aprà, E. (1994). *Ab initio* study of MnO and NiO. *Physical Review B*, Vol. 50, No.8, (August 1994), pp. 5041-5054, ISSN: 1550-235X

Zhou, W.; Ran, R. & Shao Z. (2009). Progress in understanding and development of $Ba_{0.5}Sr_{0.5}Co_{0.8}Fe_{0.2}O_{3-\delta}$-based cathodes for intermediate-temperature solid-oxide fuel cells: A review. *Journal of Power Sources*, Vol.192, No. 2, (July 2009), pp. 231-246, ISSN: 0378-7753

Wagner, C. & Schottky, W. (1930). *Z. Phys. Chemie* B, Vol. 11, No., (1930) pp. 163-, ISSN

Wagner, C. (1936). *Z. Phys. Chem*. B Vol. 32, No., (1936), pp. 447- , ISSN

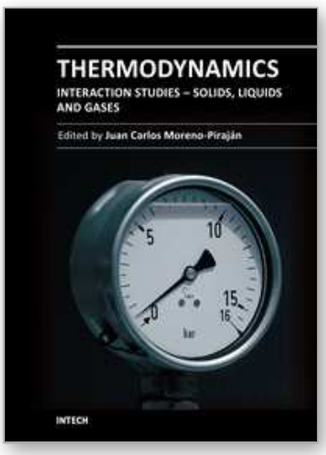

Thermodynamics - Interaction Studies - Solids, Liquids and Gases
Edited by Dr. Juan Carlos Moreno PirajÃ¡n

ISBN 978-953-307-563-1
Hard cover, 918 pages
Publisher InTech
Published online 02, November, 2011
Published in print edition November, 2011

Thermodynamics is one of the most exciting branches of physical chemistry which has greatly contributed to the modern science. Being concentrated on a wide range of applications of thermodynamics, this book gathers a series of contributions by the finest scientists in the world, gathered in an orderly manner. It can be used in post-graduate courses for students and as a reference book, as it is written in a language pleasing to the reader. It can also serve as a reference material for researchers to whom the thermodynamics is one of the area of interest.

How to reference
In order to correctly reference this scholarly work, feel free to copy and paste the following:

Eugene Heifets, Eugene A. Kotomin, Yuri A. Mastrikov, Sergej Piskunov and Joachim Maier (2011). Thermodynamics of ABO3-Type Perovskite Surfaces, Thermodynamics - Interaction Studies - Solids, Liquids and Gases, Dr. Juan Carlos Moreno PirajÃ¡n (Ed.), ISBN: 978-953-307-563-1, InTech, Available from: http://www.intechopen.com/books/thermodynamics-interaction-studies-solids-liquids-and-gases/thermodynamics-of-abo3-type-perovskite-surfaces

INTECH
open science | open minds

InTech Europe
University Campus STeP Ri
Slavka Krautzeka 83/A
51000 Rijeka, Croatia
Phone: +385 (51) 770 447
Fax: +385 (51) 686 166
www.intechopen.com

InTech China
Unit 405, Office Block, Hotel Equatorial Shanghai
No.65, Yan An Road (West), Shanghai, 200040, China
中国上海市延安西路65号上海国际贵都大饭店办公楼405单元
Phone: +86-21-62489820
Fax: +86-21-62489821

IntechOpen